

## Environmental Effects on the Galaxy Stellar Mass Function at $z \sim 2.5$

DEREK SIKORSKI,<sup>1</sup> ROY GAL,<sup>1</sup> BRIAN LEMAUX,<sup>2</sup> BEN FORREST,<sup>3</sup> EKTA SHAH,<sup>3</sup> LU SHEN,<sup>3</sup> AND LORI LUBIN<sup>3</sup>

<sup>1</sup>*Institute for Astronomy, University of Hawai‘i, 2680 Woodlawn Drive, Honolulu, HI 96822, USA*

<sup>2</sup>*Gemini Observatory, NSF’s NOIRLab 670 N. A‘ohoku Place, Hilo, HI 96720, USA*

<sup>3</sup>*Department of Physics and Astronomy, University of California, One Shields Ave., Davis, CA 95616, USA*

### ABSTRACT

We investigate the relationship between local-overdensity and the galaxy stellar mass function (SMF) for the Hyperion proto-supercluster at  $z \sim 2.5$ . With a mix of COSMOS2020 photometry and  $> 2500$  spectra, we are able to map the structure of Hyperion and its multiple extremely overdense peaks. We find the shape of the SMF depends on local-overdensity and is typically flatter in the most overdense regions, showing a higher ratio of high-to-low mass galaxies than in the field. This result is consistent with similar works in the literature, and may indicate processing of galaxies at this redshift in proto-structures is driven through galaxy mergers.

### 1. INTRODUCTION

Historically, galaxies are observed to populate two distinct classes: those that are bluer, more spiral-like, and have active star formation with moderate-to-high star formation rates (SFRs); and those that are redder, more elliptical, and have little-to-no active star formation. In addition to the bimodality of stellar properties, observations in the local universe paint a picture in which the “red-and-dead” elliptical galaxies tend to inhabit denser environments - such as groups and clusters - compared to their blue, star-forming analogues. Although efforts have been made to characterize the dominant mechanisms that lead to the quenching of (i.e. cessation of star formation in) star-forming galaxies, it is vital we understand how these mechanisms which drive star-forming galaxies to quiescence evolve with redshift. Previous studies have attempted to trace quenching in the local universe (e.g., Peng et al. 2010) and out to moderate redshifts of  $z < 2$  (e.g., Kawinwanichakij et al. 2017; Tomczak et al. 2017; Papovich et al. 2018; Webb et al. 2020; van der Burg et al. 2020), but the mechanisms responsible for the development of quiescence - and the enhanced star formation that must precede it - in the high-redshift regime ( $z > 2$ ) remain largely ambiguous.

Broadly speaking, the physical mechanisms that drive galaxy quenching can be categorized into two distinct processes: “mass quenching” or “environmental quenching” (Peng et al. 2010). As suggested by the name, mass quenching encapsulates processes that are directly correlated with the stellar or halo mass of the galaxy itself. Examples may include feedback from supernovae and stellar winds (e.g., Dekel & Silk 1986), feedback from ac-

tive galactic nuclei (e.g., Somerville et al. 2008), and the shock-heating of cold gas inflows in halos above a given mass (Dekel & Birnboim 2006). On the other hand, environmental quenching are processes linked to properties of the environment in which the galaxy is situated. These processes preferentially occur in overdense environments (such as galaxy clusters), and include mechanisms such as the stripping of circumgalactic gas via ram pressure as a result of a galaxy’s motion relative to the diffuse intracluster medium (e.g., Abadi et al. 1999), or an increased frequency of major galaxy-galaxy mergers (e.g., Lin et al. 2010), among other processes.

One of the most important and natural ways of tracking the evolution of an ensemble of galaxies is via the galaxy stellar mass function (SMF). The SMF is the volume-based number density of galaxies as a function of stellar mass, and is affected by both mass and environmental quenching mechanisms in various ways. Using SDSS ( $z < 0.1$ ) and zCOSMOS ( $0.3 < z < 0.6$ ), Peng et al. (2010) show that the ways in which the SMF is affected by mass and environmental quenching mechanisms are largely separable. This means there are environmental mechanisms that act to increase the quiescent fraction of galaxies, independent of the mass of the galaxies, and vice versa.

On the other hand, it has become more apparent that at higher redshifts ( $0.5 < z < 2.0$ ), there is a positive correlation between the overdensity of a region and the fraction of galaxies that are quiescent down to stellar masses of  $\log(M_*/M_\odot) \gtrsim 9.5$  (e.g., Kawinwanichakij et al. 2017; Tomczak et al. 2017; Papovich et al. 2018; Webb et al. 2020; van der Burg et al. 2020). Additionally, it has been shown that the environmental quench-

ing mechanisms that drive this correlation become more efficient for higher mass galaxies (Papovich et al. 2018; van der Burg et al. 2020; Webb et al. 2020), suggesting that environmental and mass quenching do not act independently of one another. Despite this, the processes responsible for environmental quenching remain unclear.

In this study, we use a mix of photometry, ground-based spectroscopy, and targeted *HST* grism spectroscopy to create a stellar mass function (SMF) for the Hyperion proto-supercluster at  $z \sim 2.5$ . By comparing SMFs of galaxies in the overdense regions of Hyperion with the SMF of field galaxies at similar redshifts, we can constrain the importance of environmental quenching mechanisms in high-redshift overdense regions. Additionally, by comparing the environmental dependencies of the SMF of Hyperion with the SMF of overdense regions at lower redshifts, we can constrain the timescales over which certain environmental quenching mechanisms must act. In doing so, we can develop a better understanding of the environmental quenching mechanisms that dominate at higher redshifts, the interplay of these processes with the stellar mass of the galaxies they quench, and how the efficiency of these mechanisms may evolve with redshift.

The structure of this paper is as follows. In Section 2 we introduce the Hyperion proto-supercluster and the various sources of data used in this study. In Section 3 we discuss how we classify galaxy environments in terms of local overdensity. Finally, in Section 4 we construct the SMF for Hyperion and discuss its implications. Throughout this study all magnitudes are presented in the AB system (Oke & Gunn 1983; Fukugita et al. 1996). We also use a  $\Lambda$ CDM cosmology with  $H_0 = 70 \text{ km s}^{-1} \text{ Mpc}^{-1}$ ,  $\Omega_\Lambda = 0.73$ , and  $\Omega_M = 0.27$ .

## 2. DATA

The Hyperion proto-supercluster lies in the heart of the Cosmic Evolution Survey (COSMOS; Scoville et al. 2007) field. As such, this work leverages the abundant photometric and spectroscopic survey data available, as well as data from targeted spectroscopic programs and *HST* grism spectroscopy. In this section, we briefly introduce Hyperion and summarize the numerous sources of data used in our study.

### 2.1. The Hyperion Proto-Supercluster

Hyperion is a massive, overdense structure centered at  $z \sim 2.5$  with a complex and extended shape containing multiple overdensity peaks connected via filamentary structures. Many of the overdensity peaks were identified as individual proto-structures using a variety of techniques including submillimeter observations

of tightly-packed starbursting galaxies, the application of a friend-of-friends algorithm on deep spectroscopic surveys, identifying an overdensity of Ly $\alpha$  emitters, and observations of extended X-ray emission around CO-emitting galaxies (Casey et al. 2015; Diener et al. 2015; Chiang et al. 2015; Wang et al. 2016). Through the construction of a 3D Ly $\alpha$  tomographic map, Lee et al. (2016) suggested that some of the peaks may be connected in a structure they deemed “Colossus.” However it was not until Cucciati et al. (2018) that the grand scale of Hyperion was mapped using the construction of overdensity maps in the COSMOS field.

The original mapping of Hyperion and derivation of its mass and other physical properties are described in Cucciati et al. (2018), who used COSMOS2015 photometry (Laigle et al. 2016) and spectroscopy from zCOSMOS (Lilly et al. 2007) and the VIMOS Ultra Deep Survey (VUDS; Le Fèvre et al. 2015). In this study, we generate updated overdensity maps leveraging more spectroscopic redshifts (see Lemaux et al. 2022) and updated catalogs of objects (see below). With these updated maps, more data, and our definition of a proto-structure (see Section 3.2, we identify Hyperion as a system of highly-overdense regions laying roughly in the region  $149.64^\circ \leq \text{RA} \leq 150.48^\circ$ ,  $2.01^\circ \leq \text{Dec} \leq 2.57^\circ$ , and  $2.35 \leq z \leq 2.70$  (see Figure 1).

Though Hyperion extends over a volume of roughly  $\sim 420 \times 55 \times 85 \text{ cMpc}^3$ , its true volume is much smaller due to its irregular shape, at roughly  $\sim 9.6 \times 10^4 \text{ cMpc}^3$ . While the entirety of Hyperion is quite overdense compared to other regions at similar redshifts, it contains 7 independent “peaks” with extreme overdensities, all of which lay at  $2.35 < z < 2.55$ . Many of these overdensity peaks were the parts of Hyperion identified in earlier studies (e.g., Casey et al. 2015; Diener et al. 2015; Chiang et al. 2015; Wang et al. 2016; Lee et al. 2016), and are summarized in (Cucciati et al. 2018). The total mass of Hyperion is estimated to be  $\sim 5.1 \times 10^{15} M_\odot$ , with the most massive of the peaks, “Theia,” having an estimated total mass of  $\sim 2.02 \times 10^{14} M_\odot$ . **It should be noted that these values depend on the overdensity-threshold used in defining Hyperion. However, with any reasonable choice, Hyperion remains one of the most massive and extended objects in this epoch** (though see Shen et al. 2021; Forrest et al. 2023; Shah et al. 2024; Staab et al. 2024, for other massive structures).

Historically, the terms like “proto-structure,” “proto-cluster,” and proto-supercluster” have been used in the literature to describe a myriad of objects. It is therefore useful to briefly define what we mean by the term “proto-supercluster” in the context of our study. We re-

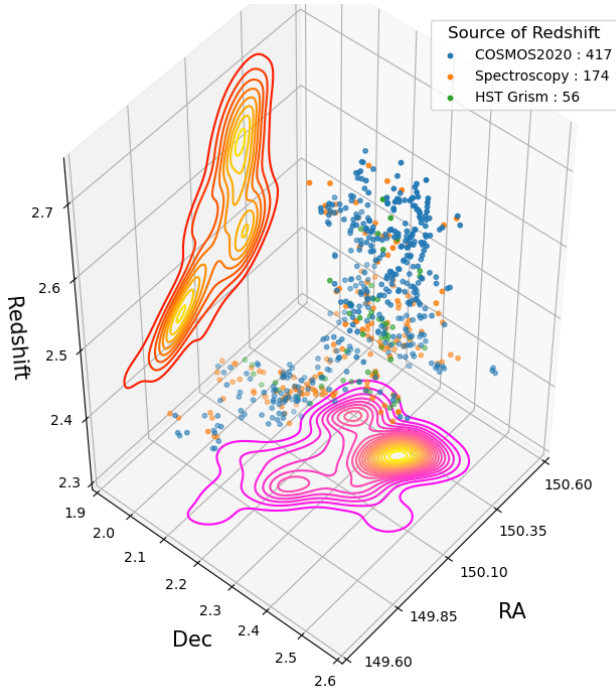


**Figure 1. The Structure of Hyperion** – A 3D map of the Hyperion proto-supercluster and a distribution of objects used in this study. Hyperion has a total mass of roughly  $\sim 5.1 \times 10^{15} M_{\odot}$  and a volume of roughly  $\sim 9.6 \times 10^4 \text{ cMpc}^3$ .

fer to Hyperion as a *proto-supercluster* (as opposed to a *proto-structure*) because its volume and mass are comparable to superclusters in the local universe, and it has a complex structure containing gravitationally interacting overdensity peaks. On the other hand, the individual peaks of Hyperion appear to be un-virialized, suggesting they are still dynamically evolving (Wang et al. 2016; Cucciati et al. 2018). Additionally, the 7 peaks appear to contain only  $\sim 10\%$  of the total mass of Hyperion. Since “superclusters” are traditionally structures with embedded clusters, each of which have a fully-formed intracluster medium and contain much of the mass of the supercluster, we refer to this instead as a “proto-supercluster” to highlight that many of the overdensity peaks are still growing. Using constrained cosmological simulations (designed specifically to match some observations), Ata et al. (2022) show by  $z = 0$  that, while the constituent overdensity peaks of Hyperion are unlikely to merge into one cluster at any point, Hyperion as a whole is likely to evolve into a massive, extended, filamentary group of clusters (see Figure 3 of Ata et al. 2022).

## 2.2. COSMOS2020 Photometry

The photometric measurements used in this work are taken from the recently-compiled COSMOS2020 cata-

logs (Weaver et al. 2022). These catalogs contain extensive data for  $\sim 1.7$  million objects spanning  $\sim 2 \text{ deg}^2$ , including imaging in up to 40 bandpasses and physical properties estimated from two SED-fitting codes. For this work, we specifically use the COSMOS2020 Classic catalog and physical parameters derived via LePhare<sup>1</sup> (Arnouts et al. 1999; Ilbert et al. 2006).

The COSMOS2020 photometry spans a wide wavelength range, from the far-UV (FUV) to the mid-infrared (MIR). A summary of the instruments and band-passes used in the catalog is provided in Table 1 of Weaver et al. (2022); and we will additionally provide a brief summary of the data. Space-based imaging includes FUV and near-UV (NUV) data from the Galaxy Evolution Explorer (GALEX; Zamojski et al. 2007), optical data from the *HST*/ACS F814W band (Leauthaud et al. 2007), and MIR data from *Spitzer*/IRAC channels 1-4 (Ashby et al. 2013, 2015, 2018; Steinhardt et al. 2014). Ground-based imaging includes NUV data from the  $u/u^*$ -bands via the MegaCam instrument on the Canada-France-Hawai‘i Telescope (CFHT; Laigle et al. 2016; Sawicki et al. 2019), optical data from 7 broad-, 12 medium-, and 2 narrowbands via Subaru/Suprime-Cam (Taniguchi et al. 2007, 2015), optical data from the *grizy*-bands via Subaru/Hyper Suprime-Cam (Aihara et al. 2019), and near-infrared (NIR) data from the  $YJHK_s$  broadbands and NB118 narrowband via the UltraVISTA survey (McCracken et al. 2012; Moneti et al. 2023). Astrometric measurements are based on data from GAIA DR1 and DR2 (Gaia Collaboration et al. 2016, 2018).

In the work that follows, we use flux densities for all bands when available, other than the *HST*/ACS band and IRAC channels 3 and 4. Specifically, for a given band XXXX, we use the flux-density reported under XXXX\_FLUX\_APER3 in the COSMOS2020 catalog and its associated error, which was found using SExtractor using a 3” aperture. A source-dependent correction given by total\_off3 is applied to the flux-density in all bands taken from ground-based observations in order to convert aperture fluxes into total fluxes. Finally, a foreground attenuation correction is applied using an extinction term, given by EBV\_MW, and a multiplicative band-dependent factor, as described in Laigle et al. (2016).

Of the  $\sim 1.7$  million photometric sources in COSMOS2020, 19,258 are missing one or more of 1p\_zPDF, 1p\_zPDF\_168, or 1p\_zPDF\_u68. As we use these three statistics to reproduce a redshift PDF (see Section 4.1), we remove these objects from our sample. Addition-

<sup>1</sup> Visit LePhare’s website [here](https://lephare.univ-poitiers.fr/~maurog/).

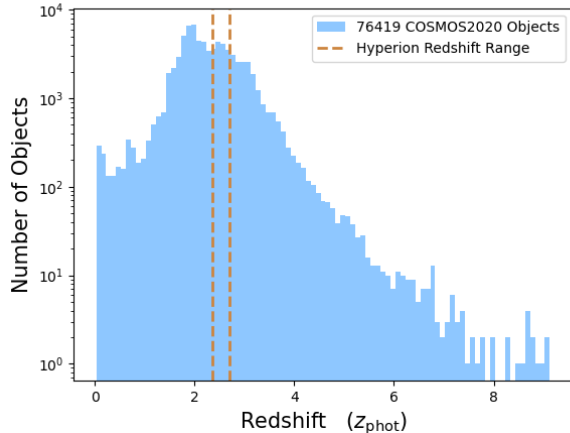


**Figure 2. Redshift Distribution of Photometry** – The redshift distribution of the 76,419 objects used in this study from the COSMOS2020 catalog after applying the cuts in Section 2.2. Note that these are the objects that have their redshift PDFs sampled during the Monte Carlo process (see Section 4.1).

ally, when building the stellar mass functions, we limit our sample to objects which have either  $[3.6] \leq 25.0$  or  $[4.5] \leq 25.0$ , which lay in the ranges  $149.60^\circ \leq \text{RA} \leq 150.52^\circ$  and  $1.74^\circ \leq \text{Dec} \leq 2.73^\circ$ , and which were determined to be either a galaxy or X-ray source in **LePhare** (`lp_type` = 0 or 2). These additional constraints limit the sample to 239,152 objects.

While the RA and Dec of the remaining objects are generally well-constrained, the redshift can be harder to pin down given the complexity of SED-fitting. To account for this, we use a set of Monte Carlo (MC) realizations in which we sample the redshift probability distribution functions (PDFs) of the objects used to create the SMFs (see Section 4.1). Therefore, rather than applying a strict redshift constraint to our data, we instead limit the sample to objects which have a non-negligible portion of their redshift PDF laying in the redshift range of interest. Specifically, we use only objects which have a median redshift ( $z_{\text{med}}$ ) no more than 3 standard deviations from the redshift range  $2 \leq z \leq 3$ . We call the lower- and upper-bounds of the 68% confidence-interval for the redshift reported by **LePhare** (`lp_zPDF_l68` and `lp_zPDF_u68` in COSMOS2020)  $\sigma_{16}$  and  $\sigma_{84}$  respectively. Then, this redshift cut is equivalent to  $(2 - z_{\text{med}})/(z_{\text{med}} - \sigma_{16}) \leq 3$  in the case  $z_{\text{med}} \leq 2$ , and  $(z_{\text{med}} - 3)/(\sigma_{84} - z_{\text{med}}) \leq 3$  in the case  $z_{\text{med}} \geq 3$ . This final cut mostly removes lower-redshift objects with narrow redshift PDFs, and further limits our sample to 76,419 objects. The redshift distribution of these objects is shown in Figure 2.

## 2.3. Spectroscopy

### 2.3.1. Wide-Scale Ground-Based Spectroscopy

There have been a number of spectroscopic surveys which have added to the wealth of data in the COSMOS field. The zCOSMOS survey (Lilly et al. 2007) is the culmination of 600 hours of observations using the VIMOS spectrograph on the VLT. zCOSMOS was split into two separate components: zCOSMOS-bright and zCOSMOS-deep. The zCOSMOS-bright component consisted of a magnitude-limited sample of galaxies in the redshift range  $0.1 < z < 1.2$ , while the zCOSMOS-deep component consisted of  $\sim 10,000$  color-selected galaxies in the redshift range  $1.4 < z < 3.0$  within the central  $1 \text{ deg}^2$  of the COSMOS field. Also taken on VIMOS was the VIMOS Ultra Deep Survey (VUDS; Le Fèvre et al. 2015), which includes spectroscopy of  $\sim 10,000$  galaxies with  $i < 25$ , spanning over a redshift range of  $2 < z < 6$ . Additionally, the DEIMOS 10k survey (Hasinger et al. 2018) using the Deep Imaging Multi-Object Spectrograph (DEIMOS) (Faber et al. 2003) on the Keck II telescope took spectra of over 10,000 objects in the redshift range of  $0 < z < 6$  with  $i < 23$ .

zCOSMOS and VUDS follow a similar system for assigning quality flags to the spectroscopic redshifts, based on Section 6.5 of Le Fèvre et al. (2005). In an effort to compare data quality, the flags of the DEIMOS 10k survey were also conformed to fit the same system (Lemaux et al. 2022). Briefly, objects are assigned a flag from 0, 1, 2, 3, 4, or 9 to indicate the confidence of the redshift measurement. In this work, we consider redshift measurements with flags 3 and 4 to be reliable  $\sim 99.3\%$  of the time, and those with flags 2 and 9 to be reliable  $\sim 70\%$  of the time (see Appendix A of Lemaux et al. 2022). Flag 1 indicated tentative redshift measurements, and thus will not be used for this work. Each quality flag can be prepended with additional flags in order to indicate if the object is peculiar in some way. For example, a quality flag of 13 would indicate a broadline AGN (per the prepended 1) with a secure redshift. As we are not interested in the specifics of these objects, we ignore the prepended flags and only consider spectra which were assigned quality flags ending with 2, 3, 4, or 9 regardless of what is prepended.

Galaxies from the zCOSMOS and VUDS surveys contribute the majority of spectroscopy in our study. We consider only objects in the RA-Dec range of Hyperion and the redshift range  $2 \leq z \leq 3$ , have a spectroscopic reliability  $\gtrsim 70\%$ , have matched COSMOS2020 photometry, and have either  $[3.6] \leq 25.0$  or  $[4.5] \leq 25.0$  (from COSMOS2020). For objects which were targeted in both surveys, we keep only the observation with the



highest spectroscopic quality flag. In the case of a tie between the quality flags, based on a hierarchy of the surveys (Forrest et al. 2023). With these restrictions, our sample contains spectroscopic redshifts for spectra of 875 zCOSMOS objects, 972 VUDS objects, and 68 DEIMOS 10K objects with matched COSMOS2020 photometry (see Figure 3).

### 2.3.2. Dedicated Follow Up Ground-Based Spectroscopy

In this work, we also incorporate data from a number of spectroscopic surveys specifically targeting over-dense proto-structure candidates. Specifically, with the use of the DEIMOS (Faber et al. 2003) and Multi-Object Spectrometer For Infra-Red Explorations (MOS-FIRE; McLean et al. 2012) instruments on the Keck telescopes, the Charting Cluster Construction with VUDS (Le Fèvre et al. 2015) and ORELSE (Lubin et al. 2009) survey (C3VO; Lemaux et al. 2022) has followed-up  $\sim 2000$  objects across three different fields. Using the Voronoi Tessellation Monte Carlo (VMC) method to identify proto-structures in existing VUDS spectroscopy, C3VO has obtained follow-up spectroscopy for a number of high-redshift proto-structures, allowing for more complete mapping of the systems. Other than Hyperion, these observations targeted a number of structures including PCl J1000+0200 ( $z \sim 2.90$ ; Cucciati et al. 2014), PCl J0227-0421 ( $z \sim 3.31$ ; Lemaux et al. 2014; Shen et al. 2021), Elentári ( $z \sim 3.33$ ; McConachie et al. 2022; Forrest et al. 2023), Smruti ( $z \sim 3.47$ ; Forrest et al. 2017; Shah et al. 2024), and Taralay ( $z \sim 4.57$ ; Lemaux et al. 2018; Staab et al. 2024).

Details regarding these observations are outlined in Lemaux et al. (2022). Briefly, the surveys targeted star-forming galaxies to  $i < 25.3$  with Keck/DEIMOS and  $H < 24.0$  with Keck/MOSFIRE, and Ly $\alpha$  emitters to even fainter magnitudes. Additionally, quality flags were assigned in a similar way to the VUDS and zCOSMOS surveys described in the previous section. For this study, the C3VO DEIMOS and MOS-FIRE programs contribute 33 and 121 objects with associated COSMOS2020 photometry, respectively, which lay in the ranges  $149.60^\circ \leq \text{RA} \leq 150.52^\circ$  and  $1.74^\circ \leq \text{Dec} \leq 2.73^\circ$ , the redshift range  $2 \leq z \leq 3$ , have either  $[3.6] \leq 25.0$  or  $[4.5] \leq 25.0$  (per COSMOS2020), and with spectroscopic reliability  $\gtrsim 99.5\%$  (see Figure 3).

In addition to these recent targeted surveys, we use a number of observations from previous studies which targeted individual peaks of Hyperion. Specifically, we use 4 spectra from Casey et al. (2015), 4 spectra from Chiang et al. (2015), and 1 spectrum from Diener et al. (2015). Details regarding the specifics of the observation programs and data reductions can be found in the

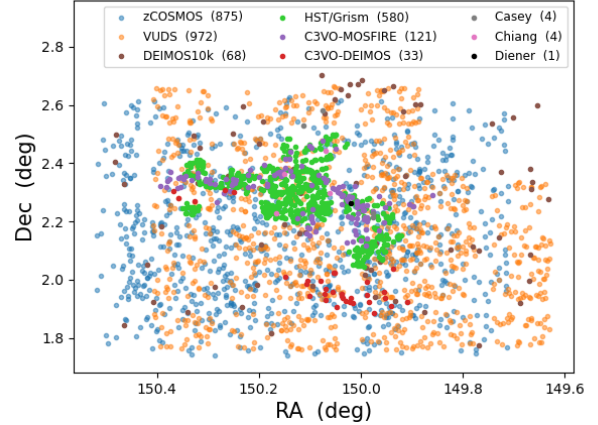


**Figure 3. Spectroscopic and HST/Grism Targets** – The projected distribution of spectroscopic observations used in this study in the redshift range  $2 < z < 3$ . The colors correspond to different surveys, with the number of objects contributed to our study given in the legend.

associated publications. Each of these spectra were examined and given a quality flag according to the same criteria as described above, and fall in the same RA-Dec and redshift range as the other observations used in this study (see Figure 3).

### 2.4. HST Grism

In addition to the COSMOS2020 photometry and ground-based spectroscopy, we use *HST* grism spectroscopy to greatly increase the number of secure redshifts in our sample. Details regarding target selection, data reduction, and redshift classification will be provided in Forrest et al., in prep., but we briefly outline the relevant information here. *HST*-Hyperion was an *HST* Cycle 29 program (PI: Lemaux) which obtained 50 orbits of WFC3/G141 slitless spectroscopy with WFC3/F160W imaging in 25 pointings covering the densest peaks in Hyperion. In total, the observations resulted in  $\sim 12,800$  spectra for objects with  $m_{\text{NIR}} < 25$ .

Given the nature of slitless spectroscopy, a number of low- and high-redshift objects also fell within the observations. In order to verify the quality of the spectrum and redshift-fit, each spectrum was visually examined by at least two members of the group. Each group member numerically classified the quality of the spectral data, the quality of the redshift fit for the object, and the quality of the SED fit to the COSMOS2020 photometry. In total, each group member classified  $\sim 2500$  spectra. After all spectra were classified, the classifications for each object were compared to each other. If there was a drastic difference between the classification (i.e. one deemed the redshift usable and the other did not),

the classifiers for that object met and discussed which decision to uphold.

Once all spectra had agreed-upon flags, a final quality flag was assigned to each object, ranging from 0 (lowest quality) to 5 (highest quality). To calibrate the reliability of the quality flags, we compared the *HST* grism redshift ( $z_g$ ) with the ground-based spectroscopic redshift ( $z_s$ ) for objects with both measurements. To ensure the data was reasonably good, we only considered grism spectra with flags  $\geq 3$  and ground-based spectra with quality flags of 3 or 4 (see Section 2.3.1). Given the extremely high reliability for the ground-based spectra, we treated  $z_s$  as the true redshift and examined the distribution of  $(z_g - z_s)/(1 + z_s) = \Delta z/(1 + z_s)$ . We calculated the normalized median absolute deviation ( $\sigma_{\text{NMAD}}$ ; Hoaglin et al. 1983), a measure of the distribution’s width which is more robust to outliers. Denoting the median of a value  $x$  as  $\text{Med}(x)$ ,  $\sigma_{\text{NMAD}}$  is given as

$$\sigma_{\text{NMAD}} = 1.48 \times \text{Med} \left( \frac{|\Delta z - \text{Med}(\Delta z)|}{1 + z_s} \right). \quad (1)$$

For the combined samples of grism redshifts with quality flags  $\geq 3$ , we find  $\sigma_{\text{NMAD}} \approx 0.0019$ . For a galaxy at  $z = 2.5$ , this corresponds to a wavelength offset of  $\sim 22 \text{ \AA}$ . In general, we then assume  $\Delta z/(1 + z_s) < 0.004$  and compute the proportion of grism spectra which fall within this cutoff for each quality flag to determine the reliability of the quality flag. For quality flags 3, 4, and 5, we find 56.7%, 77.3%, and 90.4% of galaxies which have  $\Delta z/(1 + z_s) < 0.004$ , thus defining the reliability of the flags. In Figure 3, we show the objects with grism spectroscopy in the redshift range  $2 \leq z \leq 3$  which have a quality flag  $\geq 3$ . Note that for objects with both a  $z_s$  and  $z_g$ , we show only the measurement with the highest reliability. However, both measurements are used in our analysis (see Section 4.1).

### 3. CHARACTERIZING GALAXY ENVIRONMENTS

Developing a quantitative method to describe the environment in which a galaxy resides is central to understanding the environmental effects on galaxy evolution. While there are a variety of methods used to quantify local environments, we employed a Voronoi Tessellation Monte Carlo mapping technique which has been proven successful in many previous works (e.g., Tomczak et al. 2017; Cucciati et al. 2018; Hung et al. 2020; Shen et al. 2021; Lemaux et al. 2022; Forrest et al. 2023; Staab et al. 2024). The method produces a 3D grid of voxels, each with an associated overdensity value, to which galaxies are assigned. From these maps, we can

identify extended, connected regions of voxels exceeding a given overdensity threshold, which are taken to be proto-structures. In this section, we briefly explain the Voronoi Tessellation Monte Carlo mapping technique before discussing the specific details of the map used in this study.

#### 3.1. Generating Overdensity Maps

##### 3.1.1. The Voronoi Tessellation Monte Carlo Method

The Voronoi Tessellation Monte Carlo (VMC) algorithm leverages a combination of well-constrained spectroscopic redshifts and less-constrained photometric redshifts to statistically map the 3D spatial distribution of galaxies. Broadly speaking, a Voronoi tessellation map divides a plane into polygons, where each polygon is centered on a specific point in a given distribution. These polygons encompass all locations in the plane that are closer to their corresponding point than to any other point in the distribution, effectively partitioning the plane based on proximity. In the context of mapping galaxy density fields, the polygons partition two dimensions (RA and Dec) based on proximity to the closest galaxy (see left panel of Figure 4).

Given the size of the uncertainties for the photometric redshifts as well as the sparseness of the spectroscopic sample, this method cannot be directly applied in the redshift dimension. Instead, the tessellation maps are constructed in the 2D RA-Dec plane in overlapping redshift slices. A set of Monte Carlo realizations is generated for each redshift slice of the 3D space in order to minimize the effects of photometric redshift uncertainties by better sampling the redshift PDF. In a given realization, each galaxy in the data set is assigned a redshift based on the following logic:

1. For galaxies which do not have a measured spectroscopic redshift, a new redshift is drawn from an asymmetric Gaussian distribution centered on the reported photometric redshift and with lower/upper standard deviations equal to the lower/upper uncertainties ascribed to their redshift probability distributions.
2. For galaxies with a measured spectroscopic redshift, a random number is drawn from a uniform distribution ranging from 0 to 100. If the number is less than or equal to the reliability associated with the quality-flag of the spectroscopic redshift (e.g.  $\leq 70$  for flags X2/X9), the reported spectroscopic redshift is kept. Otherwise, a new redshift is drawn from the photometric redshift distribution, as described above.

Only the galaxies assigned redshifts in the given redshift slice are kept for each realization, and a 2D Voronoi tessellation is performed to create a 2D polygon map (see Figure 4). The density associated with a polygon,  $\Sigma_{\alpha,\delta,z}$ , is then inversely proportional to its area in  $\text{Mpc}^2$ . This is re-mapped onto a consistent grid of voxels in RA-Dec space separated by 75 pkpc, where each voxel has the density of the polygon enclosing its center in the given Monte Carlo realization.

### 3.1.2. Applying the VMC Method

The VMC maps used in this study are described in Lemaux et al. (2022), and thus we give only a brief description here. The maps used in this study were generated using the COSMOS2015 photometry (Laigle et al. 2016) and associated field spectroscopic surveys (described in Section 2.3). The VMC process, as described above, was performed over the entire COSMOS footprint for redshifts  $2 \leq z \leq 5$ . The redshift bins had widths of 7.5 Mpc, with overlaps of 90% between adjacent redshift slices. A total of 100 MC realizations were performed for each redshift slice to generate the map, using only those galaxies that fell within the redshift bin and with magnitudes  $[3.6] < 24.8$  for the density calculations in a given realization. Afterwards, each voxel was assigned a density  $\Sigma_{\alpha,\delta,z}$  equal to the median density of that voxel across all MC realizations.

The density measurement found via VMC mapping is subject to differences in the quality of data used, magnitude cuts, and other observational constraints (see Hung et al., in prep). Additionally, the average density of the Universe evolves with redshift and can be difficult to quantify directly. Because we are interested in quantifying galaxy evolution with respect to the surrounding environment and comparing this to the evolution at other redshifts, it is more useful to use the local overdensity,  $\log(1 + \delta_{\text{gal}})$ , rather than just density, as an environmental metric. Given the density of a voxel  $\Sigma_{\alpha,\delta,z}$ , and the average density for the redshift slice containing the voxel,  $\langle \Sigma_z \rangle$ , the overdensity of the voxel, is defined as

$$\log(1 + \delta_{\text{gal}}) \equiv \log \left( 1 + \frac{\Sigma_{\alpha,\delta,z}}{\langle \Sigma_z \rangle} \right). \quad (2)$$

In order to find  $\langle \Sigma_z \rangle$ , the outer 10% of voxels in each redshift slice are first trimmed to mitigate edge effects. The remaining 2D density distribution in the redshift slice,  $\Sigma_z$ , is then smoothed with a 2D-Gaussian kernel with standard deviations of  $3\sigma$  in the two spatial dimensions (RA and Dec). Since  $\Sigma_z$  roughly follows a log-normal distribution, a Gaussian is fit to the distribution of  $\log(\Sigma_z)$  in each redshift slice. Finally, a  $2\sigma$ -clipping is applied and another Gaussian is fit, resulting in a mean  $\mu_{\Sigma}(z)$  and standard deviation  $\sigma_{\Sigma}(z)$

for each redshift slice (top left panel of Figure 5). The mean density in the redshift-bin is related to the mean and standard deviation of the log-normal distribution via  $\langle \Sigma_z \rangle = 10^{\mu} \cdot \exp(2.652\sigma^2)$ .

Once the average density is found in each redshift slice, the overdensity can be calculated for each voxel in the slice from Equation 2. As above, the distribution of  $\log(1 + \delta_{\text{gal}})$  in the slice is fit with a  $2\sigma$ -clipped Gaussian resulting in a  $\mu_{\delta}(z)$  and  $\sigma_{\delta}(z)$  for that slice (bottom left panel of Figure 5). It should be noted that, given that proto-structures are extended in redshift space over multiple redshift slices, it is possible that an entire redshift slice is over- or underdense. Thus, a 5th-order polynomial is fit to  $\mu_{\delta,z}$  and  $\sigma_{\delta,z}$  to better characterize the general variation across redshift (see right panels of Figure 5), resulting in measurements for the parameters as a function of redshift,  $\mu_{\delta,5}(z)$  and  $\sigma_{\delta,5}(z)$ .

With these in hand, we now have a metric for characterizing the local overdensity in each voxel of the VMC map by representing it as  $\log(1 + \delta_{\text{gal}}) = \mu_{\delta,5}(z) + n_{\sigma}\sigma_{\delta,5}(z)$ . With this form, the local overdensity is parameterized entirely by  $n_{\sigma}$ , or the number of  $\sigma_{\delta,5}$  above  $\mu_{\delta,5}$  the local overdensity for a given voxel. This metric is robust over cosmic fluctuations given the polynomial fit, as well as observational constraints given the MC process used to generate the underlying  $\log(1 + \delta_{\text{gal}})$  distribution.

### 3.2. Identifying proto-structures

In the context of the VMC overdensity maps, we define a “proto-structure” as a contiguous set of voxels, all of which have  $n_{\sigma} \geq 2$  (corresponding to  $\delta_{\text{gal}} \gtrsim 0.5$  at  $z \sim 2.5$ ) and which have a combined mass of  $M_{\text{tot}} \geq 10^{13} M_{\odot}$ . The mass of the voxels is estimated by using (from Steidel et al. 1998):

$$M_{\text{tot}} = \bar{\rho} V \left( 1 + \frac{\langle \delta_{\text{gal}} \rangle}{b} \right), \quad (3)$$

where  $\bar{\rho}$  is the mean comoving density of the universe,  $\langle \delta_{\text{gal}} \rangle$  is the mean overdensity of the voxels defining the peak,  $V$  is the combined volume of the voxels, and  $b$  is the bias factor, (2.55, as derived at  $z \sim 2.5$  by Durkalec et al. (2015)). It should be noted that, while this mass-estimate may be rough, in this work it’s used primarily as a method for differentiating between regions that are overdense because they are potentially proto-structures, and regions that are overdense simply due to cosmological perturbations in density.

In Figure 6, we show the distribution of barycenters (*top*) and galaxies (*bottom*) in our sample that lay in proto-structures around Hyperion. Specifically, the barycenter of Hyperion is located at RA  $\sim 150.2^{\circ}$  and

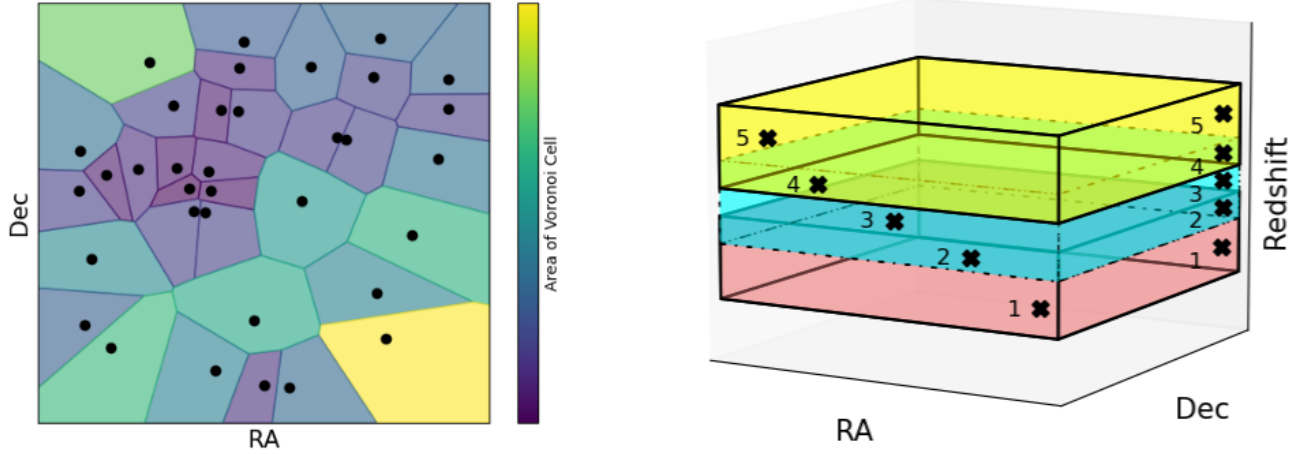


**Figure 4. VMC Map Diagram** – **Left:** A single redshift slice of the VMC map after being partitioned into Voronoi tessellations. The density of each galaxy (dots in the diagram) is related to the inverse of the area of the polygon encompassing it. **Right:** A stack of 3 overlapping redshift slices (red, cyan, and yellow). Galaxies 1, 3, and 5 are in the red, cyan, and yellow slices respectively. Galaxies 2 and 4 are in overlapping regions and thus are mapped in two different redshift slices. In practice, the redshift slices are quite thin, and overlap with 90% of the neighboring ones (rather than the  $\sim 33\%$  overlap here).

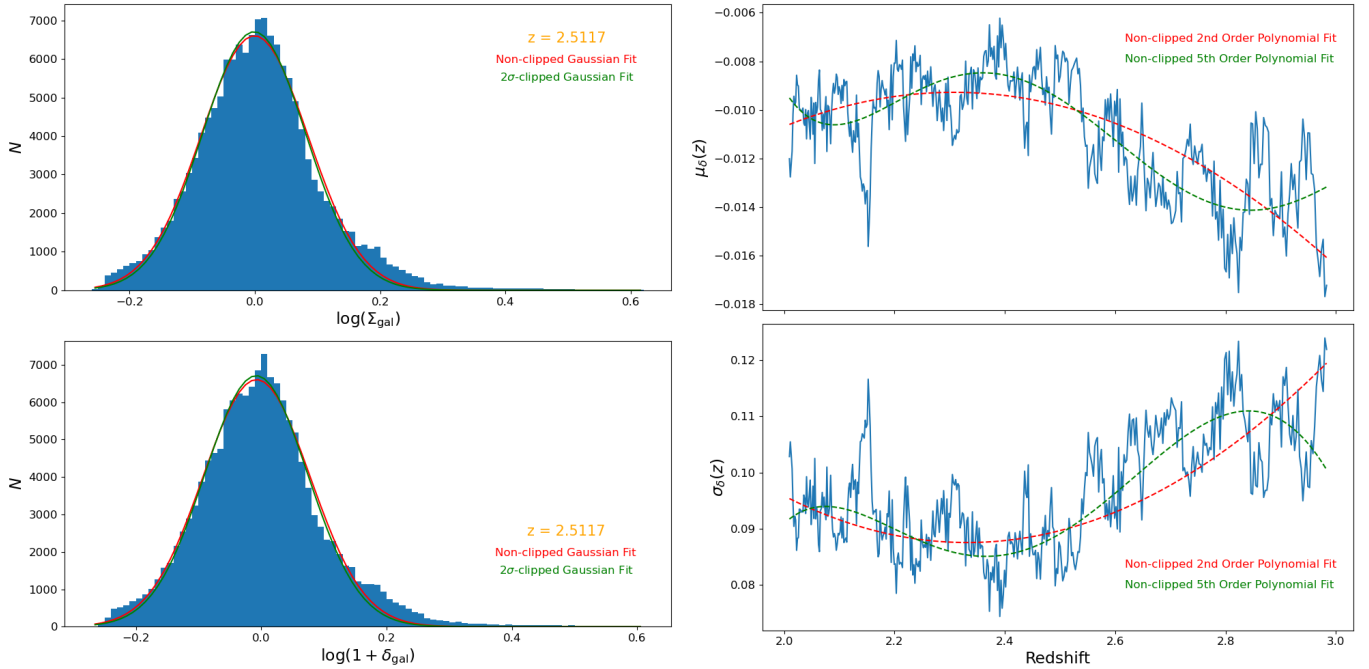


**Figure 5. Overdensity Mapping** – **Left:** The distributions (with median set to zero) of log-density (*top*), and local-overdensity (*bottom*) for all of the voxels in the redshift bin centered on  $z \sim 2.51$ . The Gaussian and  $2\sigma$ -clipped Gaussian (*red* and *green*, respectively) are fit over both distributions. **Right:** The distribution of the mean-overdensity (*top*) and standard deviation of overdensity (*bottom*) as a function of redshift. The functions are fit with 2<sup>nd</sup>- and 5<sup>th</sup>-order polynomials (*red* and *green*, respectively).



Dec  $\sim 2.3^\circ$ . Recall from our definition of a proto-structure that each of the barycenters represent structures which are completely independent from each other in the sense that they do not share any voxels in the overdensity map. This does not imply that the structures are physically evolving completely independently from each other (they very well could be interacting gravitationally), but we treat them as independent from Hyperion in our analysis. The structure of Hyperion is shown in Figure 1.

By varying our  $n_\sigma$ -threshold, we can isolate the most overdense regions of Hyperion. Particularly, Figure 7 shows the regions of Hyperion which have  $n_\sigma \geq 4.0$ . These are the most overdense peaks of Hyperion, and the regions of Hyperion in which environmental effects on galaxy evolution are expected to be the strongest. We find a total of 11 overdense peaks in Hyperion, including the most massive peak Theia. Combined, the peaks have an estimated total mass of  $\sim 5.8 \times 10^{14} M_\odot$  and volume of  $\sim 8400 \text{ cMpc}^3$ . Additionally, all of these peaks are at redshifts  $2.35 \leq z \leq 2.55$ .

### 3.3. Creating a Field Sample

In order to understand how overdense environments affect galaxy evolution, we must be able to identify a control sample of field galaxies which have evolved in lower density environments. Note that this is *not* simply the galaxies in the region surrounding Hyperion that do not fall in voxels with  $n_\sigma \geq 2$  (labelled “excluded” galaxies in Figure 6). While we do not count these as constituents of Hyperion, their evolution may still have been impacted by the denser nearby environments. Therefore, we instead look at a sample of galaxies in a region further isolated from Hyperion. Specifically, we look at two samples of galaxies in the redshift ranges  $2.15 \leq z \leq 2.25$  and  $2.80 \leq z \leq 2.90$ .

While we want to minimize the potential effects of the environment on our field samples, we must also be conscious that there may exist regions within the redshift ranges of the field sample that are overdense due to cosmic variance rather than being proto-structures. If we were to simply define the field as regions where  $n_\sigma < 2$  within these redshift ranges, we would be neglecting cosmological variations of overdensity due to perturbations in the early universe. Effects of this on galaxy evolution would be imprinted onto the SMFs of our field sample, and we would thus be unable to separate this effect from the environmental effects stemming from evolving within a proto-structure. Therefore, we try to remove only galaxies in the control sample which appear to be part of proto-structures rather than simply in overdense regions.

To do this, we remove only those galaxies in both redshift ranges which lie in regions of contiguous voxels which have a total mass greater than  $M \geq 10^{13} M_\odot$  (as calculated from Equation 3) and which have at least one voxel with  $n_\sigma \geq 4$ . That is, they lay in environments with such extreme overdensity and with a large enough mass that the environment could have non-negligible effects on galaxy evolution. Plots of the field samples are shown in Figures A1 and A2.

## 4. BUILDING THE STELLAR MASS FUNCTIONS

Despite our extensive spectroscopic data, our sample is still dominated by galaxies with relatively poorly constrained photo- $z$ ’s (see Figure 1). In theory, photometric galaxies which fall outside of the range of Hyperion could really be located in one of the peaks, changing the SMF of Hyperion, and vice versa. To extract as much information as we can from our sample we must be able to correctly quantify our uncertainty regarding which peak (if any) a galaxy is located in, by correctly accounting for each galaxy’s redshift uncertainty. However, as the stellar masses are derived via SED-fitting, the redshift of a galaxy is intricately tied to the stellar mass of the galaxy. Thus, a redshift uncertainty results not only in an uncertainty for a galaxy’s 3D location (voxel and thus overdensity), but also in the galaxy’s stellar mass.

Rather than making explicit or simplistic assumptions about how the stellar mass changes as a function of redshift, we instead try to account for this uncertainty by sampling the redshift distributions of our data via a Monte Carlo (MC) process. In this section, we describe how we generate the MC realizations and how each galaxy in a given realization is fit with a new stellar mass, before finally creating the SMFs based on the resulting galaxy distributions. It should be noted that this process is independent of the MC process used to generate the overdensity map (Section 3.1). In what follows, we sample only the redshifts of the galaxies and assign an overdensity based on the already-generated VMC map.

### 4.1. Probing Redshift Distributions

#### 4.1.1. Photometric Redshift PDFs

As all of the galaxies in our data have corresponding COSMOS2020 photometry, the photo- $z$  PDF for each galaxy is built from the reported LePhare fits in the COSMOS catalog. Specifically, we assume the PDF is a skew-normal distribution, given as (from Azzalini 1985):

$$f(z) = 2\phi(z)\Phi(\eta z) = 2\phi(z) \int_{-\infty}^{\eta z} \phi(x) dx, \quad (4)$$

where  $\phi(z)$  is a Gaussian distribution centered at redshift  $z$ ,  $\Phi(\eta z)$  is the cumulative distribution function

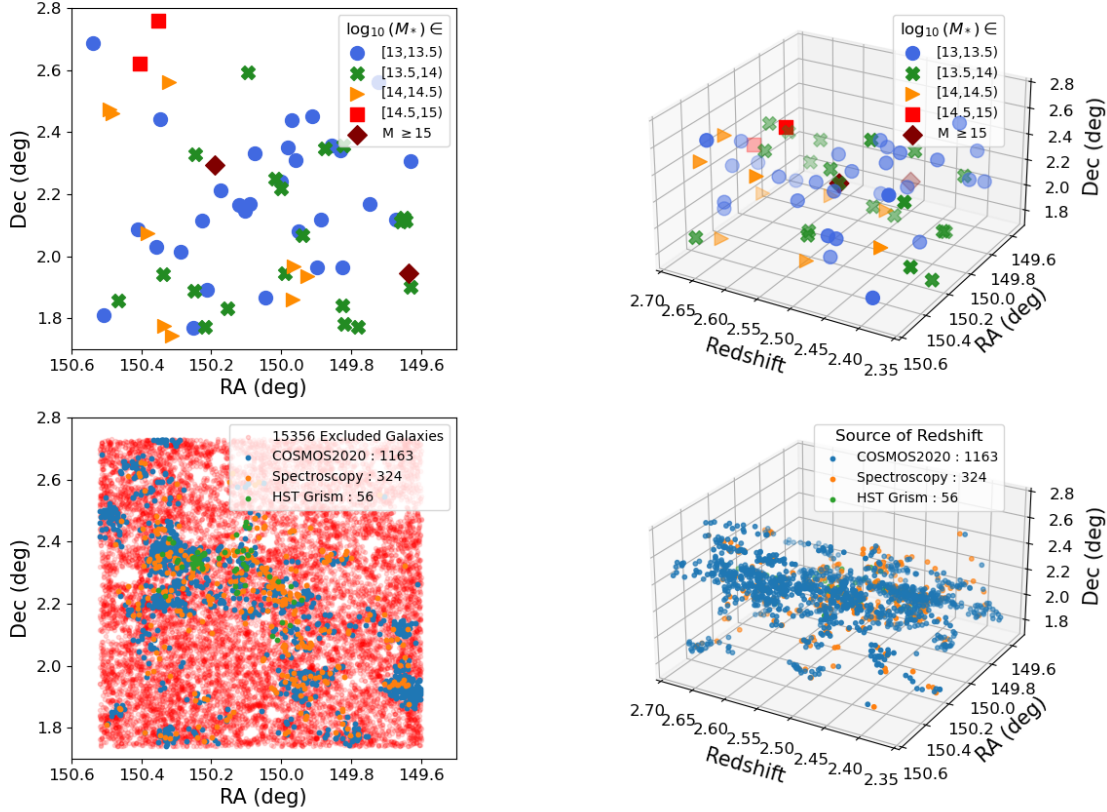


**Figure 6. Proto-Structures Around Hyperion** – **Top:** Distribution of the barycenters of the  $n_\sigma > 2$  overdensity peaks of Hyperion, in the sky-projected plane (*left*) and 3D space (*right*). **Bottom:** Distribution of galaxies that fall in voxels which have  $n_\sigma \geq 2.0$  in the sky-projected plane (*left*) and 3D space (*right*). The “excluded galaxies” in the bottom right plot are galaxies which fall in this volume, but are excluded from the structures plotted here.

of the Gaussian evaluated at  $\eta z$ , and  $\eta$  is the “shape-parameter” such that  $\eta = 0$  corresponds to  $f(z)$  being simply a Gaussian distribution. At this point, it is common to introduce a linear transformation such that  $Z = \xi + \omega z$ , where  $\xi$  and  $\omega$  are the location and scale parameter, respectively. Thus, the skew-normal PDF takes the form:

$$f(Z) = \frac{2}{\omega} \phi\left(\frac{z - \xi}{\omega}\right) \Phi\left(\eta \cdot \frac{z - \xi}{\omega}\right),$$

where the  $1/\omega$  term in front ensures that the PDF is normalized. Therefore, the skew-normal distribution can be written in terms of  $\eta$ ,  $\omega$ , and  $\xi$ . These three parameters can be related to the median (`1p_zBEST`), and lower and upper bounds of the 68% confidence interval (`1p_zPDF_l68` and `1p_zPDF_u68`) of the photometric redshift PDF reported in COSMOS2020.

With this in mind, we build a skew-normal distribution for each galaxy in our sample based on the median

redshift and lower and upper bounds of the 68% confidence interval reported in COSMOS2020. To do this, we use `scipy.optimize.minimize` (Virtanen et al. 2020) to minimize a cost-function which measures how close the median of the skew-normal is to reported median, and how close the areas between the median of the skew-normal and the lower and upper 68% confidence intervals are to 34% each. After fitting the skew-normal distributions, we keep only galaxies which have a reported median within 0.1 of the median of the skew-normal. In total, this requirement removes 234 photometric sources and 16 spectroscopic sources. Note that all objects plotted in Figure 1 meet this requirement.

#### 4.1.2. Building the Redshift Monte Carlo

In order to account for redshift uncertainties, we create a suite of 100 Monte Carlo realizations in which we attempt to well-sample the redshift PDFs of our data. Broadly speaking, our data have a photo- $z$ , spec-

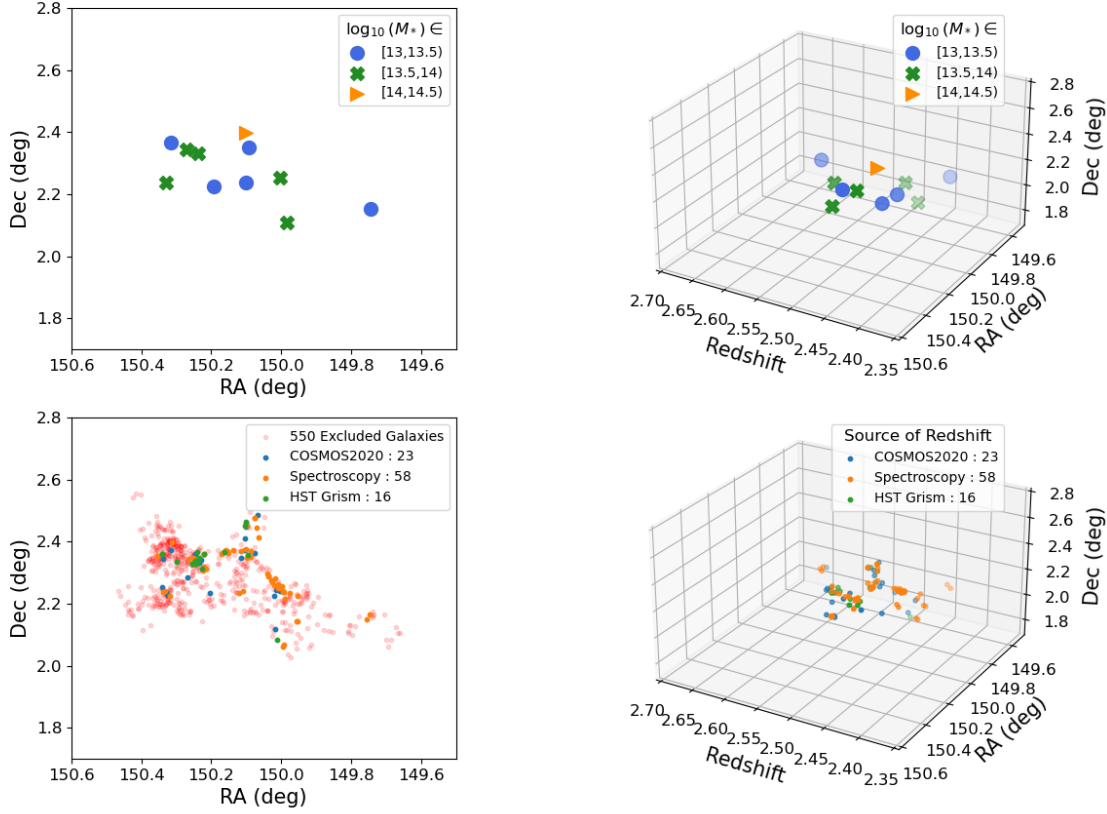


**Figure 7. Overdense Peaks of Hyperion – Top:** Distribution of the barycenters of the  $n_\sigma > 4$  overdensity peaks of Hyperion, in the sky-projected plane (*left*) and 3D space (*right*). **Bottom:** Distribution of galaxies that fall in voxels which have  $n_\sigma \geq 4.0$  in the in the sky-projected plane (*left*) and 3D space (*right*). The “excluded galaxies” in the bottom right plot are galaxies which are contained in Hyperion, but which are not in one of the overdense peaks.

$z$ , grism- $z$ , or some combination of the three. The goal then is, for galaxies with more than just a photo- $z$ , to use the more secure redshift measurement (either spec- $z$  or grism- $z$ ) a number of times which is proportional to the reliability measurement, given by the quality flag (see Section 2).

For a given galaxy in a given MC iteration, the logic for choosing a redshift depends on the combination of redshift measurements available for that galaxy. For a galaxy with all three types of redshift measurements, we could potentially draw a new redshift from three different PDFs. If based on the photo- $z$ , redshifts are randomly drawn from a skew-normal distribution,  $p(z)$ , using `scipy.stats.skewnorm` (Azzalini & Capitanio 2009; Virtanen et al. 2020) with parameters derived from the COSMOS2020 catalog, as described in the previous section. If based on the grism- $z$ , redshifts are randomly drawn from a Gaussian distribution  $g(z)$  centered on

the measured redshift from the grism spectroscopy,  $z_g$ , and with a width equal to  $\sigma_g = 46/14100 \cdot (1 + z_g)$  (motivated in Section 2.4). Finally, if based on the spec- $z$ , redshifts are simply taken to be the measured spectroscopic redshift,  $z_s$ . Thus, we outline how the random redshift,  $z_{MC}$ , is drawn based on whether the galaxy has a photo- $z$  ( $z_p$ ), spec- $z$  ( $z_s$ ), grism- $z$  ( $z_g$ ), or some combination of the three. Note, in order for it to be refit with **LePhare** given the new  $z_{MC}$ , we require each galaxy has corresponding COSMOS2020 photometry.

**Only  $z_p$ :** The vast majority of galaxies ( $\sim 92.8\%$ ) only have a photo- $z$ , which is reported in COSMOS2020. For these galaxies, we simply draw  $z_{MC} \sim p(z)$  for each MC iteration.

**$z_p$  and one of  $z_s$  or  $z_g$ :** In this case, the galaxy has COSMOS2020 photometry and either a  $z_g$  or  $z_s$ . The spec- $z$  or grism- $z$  also has an associated reliability flag corresponding to some confidence in the redshift,

$qf$  (described in Section 2). For each MC iteration, a random number,  $\mathcal{R}$ , is drawn from a uniform distribution on the half-open interval  $[0, 1)$ . If  $\mathcal{R} \geq qf$ , then we take  $z_{\text{MC}} \sim p(z)$ . Otherwise, we take  $z_{\text{MC}} = z_s$  or  $z_{\text{MC}} \sim g(z)$ , depending on whether the additional redshift is a spec- $z$  or grism- $z$ .

**$z_p$ ,  $z_s$  and  $z_g$ :** Some galaxies in our data have all three types of redshift measurements. In this case, the first step is to compare the confidence levels corresponding to the quality flags of the additional redshift measurements, which we call  $qf_s$  and  $qf_g$  for the spec- $z$  and grism- $z$ , respectively. For clarity, we define the quantity  $\mathcal{Q} \equiv qf_{\text{max}} + qf_{\text{min}} \cdot (1 - qf_{\text{max}})$ , corresponding to the  $qf_{\text{min}}$  fraction of the way between  $qf_{\text{max}}$  and 1. That is, if  $qf_{\text{max}} = 0.95$  and  $qf_{\text{min}} = 0.7$ , (corresponding to 95% and 70% confidences in the additional redshift measurements) then  $\mathcal{Q} = 0.95 + 0.7 \cdot (0.05) = 0.985$ , or 70% of the way between 0.95 and 1. This way, if the less reliable of the additional redshifts is selected in a given MC iteration, the remaining interval  $[qf_{\text{max}}, 1)$  is weighted according to the confidence associated with that less reliable measurement.

With this defined, a random number,  $\mathcal{R}$ , is drawn from a uniform distribution on the half-open interval  $[0, 1)$ , and a redshift is assigned depending on which of the additional redshift measurements has a higher confidence. In the case  $qf_{\text{max}} = qf_s > qf_g = qf_{\text{min}}$  (the spec- $z$  is more reliable than the grism- $z$ ), a redshift is assigned according to:

$$\begin{cases} \mathcal{R} < qf_{\text{max}} & \Rightarrow z_{\text{MC}} = z_s \\ qf_{\text{max}} \leq \mathcal{R} < \mathcal{Q} & \Rightarrow z_{\text{MC}} \sim g(z) \\ \mathcal{Q} \leq \mathcal{R} < 1 & \Rightarrow z_{\text{MC}} \sim p(z) \end{cases}$$

Conversely, if  $qf_{\text{max}} = qf_g > qf_s = qf_{\text{min}}$  (the grism- $z$  is more reliable than the spec- $z$ ), a redshift is assigned according to:

$$\begin{cases} \mathcal{R} < qf_{\text{max}} & \Rightarrow z_{\text{MC}} \sim g(z) \\ qf_{\text{max}} \leq \mathcal{R} < \mathcal{Q} & \Rightarrow z_{\text{MC}} = z_s \\ \mathcal{Q} \leq \mathcal{R} < 1 & \Rightarrow z_{\text{MC}} \sim p(z) \end{cases}$$

We apply this process to every galaxy in the COSMOS2020 catalog to create 100 MC realizations of our entire galaxy sample. In our analysis, we use any galaxy that appears in the redshift range of  $2 \leq z \leq 3$  in at least one MC realization.

#### 4.2. Fitting Stellar Mass

For each Monte Carlo realization, we refit the stellar mass of every galaxy based on its MC-assigned redshift.

In order to refit the masses, we use **LePhare++** with similar parameters to those used in the COSMOS2015 and COSMOS2020 catalogs (Ilbert et al. 2015; Laigle et al. 2016; Weaver et al. 2022). Since we are working with high redshift data and are interested in a statistical study of a broad population of galaxies, we use only galaxy SED templates, excluding stellar and QSO templates. In this section, we briefly discuss the parameters used for the SED fits.

The SED fitting is performed using the flux densities reported in COSMOS2020. As described in Section 2.2, for a given a band **XXXX**, we use the aperture-to-total corrected flux density reported under **XXXX\_FLUX\_APER3**, and its error from the COSMOS2020 Classic catalog. When available, we use fluxes from 35 bands including all ground-based observations, *Spitzer*/*IRAC* channels 1 and 2, and NUV and FUV data from GALEX. We apply a systematic magnitude offset to the reported photometry (**APPLY\_SYSSHIFT** in **LePhare**) given in Table 3 of Weaver et al. (2022).

To fit for the physical properties of the galaxies, we use a set of 12 SSP templates from Bruzual & Charlot (2003). For all 12 templates, we assume a Chabrier (2003) initial mass function, in which 8 templates have an exponentially declining SFH and 4 have a delayed SFH. The former have SFR e-folding time periods in the range  $0.01 \text{ Gyr} \leq \tau \leq 30 \text{ Gyr}$  and the latter have either  $\tau = 1 \text{ Gyr}$  or  $\tau = 3 \text{ Gyr}$ . Models assume either half-solar or solar metallicities. We assume two different models for attenuation for all but the templates with the lowest SFRs: one from starbursting galaxies (Calzetti et al. 2000) and one assuming a wavelength dependence of  $\lambda^{0.9}$  (Arnouts et al. 2013). We assume color-excesses of  $E(B - V) = 0., 0.05, 0.1, 0.2, 0.3, 0.5, 1$ . Dust emission is accounted for by adding flux contributions from templates via Béthermin et al. (2012) to the SSP templates. Emission lines are added to the templates using the **EMP\_UV** option in **LePhare**, which uses relations from Kennicutt (1998) to relate UV luminosity to an SFR, which in turn defines an H $\alpha$  luminosity and subsequently other line-luminosities based on predefined flux ratios (Ilbert et al. 2009). Emission lines are allowed to vary from the expected ratios by factors of 0.25, 0.5, 1, and 2, and the models are evaluated at 43 different galactic ages.

To ensure consistency of our fits with those reported in COSMOS2020, we refit galaxies in the COSMOS2020 catalog between  $2 \leq z \leq 3$  and with  $[3.6] \leq 25.0$  and/or  $[4.5] \leq 25.0$  using our parameters. In Figure 8, we show the difference in stellar mass between the COSMOS2020 mass, reported as **1p\_MASS\_MED**, and our refitted stellar mass for 37,012 galaxies. While there does appear to be



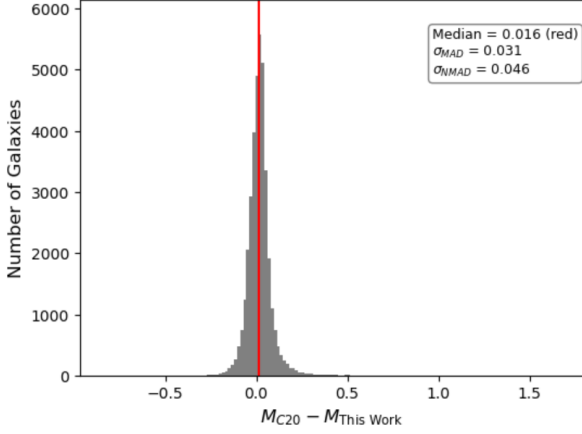


**Figure 8. Refitting COSMOS2020 Stellar Masses** – We show the difference in stellar mass between the COSMOS2020 catalog (1p\_MASS\_MED) and our LePhare outputs. The median offset and  $\sigma_{\text{NMAD}}$  (see Equation 1) are well within the expected uncertainty given the SED-fitting method.

an extremely small offset, it is well within the spread of the distribution.

#### 4.3. Creating and Fitting the Stellar Mass Functions

With these Monte Carlo realizations of our sample, we then construct stellar mass functions (SMF) for Hyperion and the field sample. To do this, we bin the galaxy populations for each of the 100 MC realization by the local overdensity of its environment and stellar mass. We choose to construct SMFs for Hyperion applying three different overdensity thresholds:  $n_\sigma \geq 2$ ,  $n_\sigma \geq 3$ , and  $n_\sigma \geq 4$ . We initially construct the SMFs for both field samples (i.e., the lower and higher redshift samples) separately, though a comparison between the two shows little difference. We therefore choose to combine these into one larger field sample. The final SMFs are shown in Figure 9. The reported values for a given stellar mass and environmental bin are the median values across the 100 MC realizations. The error bars are created by adding Poisson uncertainty and the normalized median absolute deviation of the number density for a given bin in quadrature.

We additionally fit Schechter functions to the SMFs for easier analysis with existing literature, given by (from Schechter 1976)

$$n_{\text{gal}} = \Phi d \log M \\ = \ln(10) \Phi^* \times \\ \exp \left[ -10^{\log(M) - \log(M^*)} \right] 10^{(\log(M) - \log(M^*))(1+\alpha)}.$$

The Schechter function is characterized by a power law slope,  $\alpha$ , for masses smaller than some characteristic

**Table 1. Schechter Fit Parameters** – The best fit parameters from the single-Schechter function fits for the field and Hyperion SMFs. Each SMF was fit once allowing all parameters to freely vary, and once fixing  $\alpha = -1.3$ .

Density Bin	$\log(M^*/M_\odot)$	$\alpha$	$\Phi^*/(10^{-3} \text{ Mpc}^{-3})$
Field	$11.04 \pm 0.02$	$-1.46 \pm 0.03$	$0.19 \pm 0.02$
	$10.90 \pm 0.05$	$= -1.3$	$0.33 \pm 0.04$
$n_\sigma \geq 2$	$11.38 \pm 0.27$	$-1.48 \pm 0.08$	$0.28 \pm 0.16$
	$11.03 \pm 0.08$	$= -1.3$	$0.68 \pm 0.09$
$n_\sigma \geq 3$	$11.19 \pm 0.25$	$-1.30 \pm 0.10$	$0.82 \pm 0.43$
	$11.19 \pm 0.11$	$= -1.3$	$0.82 \pm 0.11$
$n_\sigma \geq 4$	$10.96 \pm 0.24$	$-1.11 \pm 0.18$	$2.38 \pm 1.37$
	$11.28 \pm 0.21$	$= -1.3$	$1.13 \pm 0.29$

mass  $M^*$ . For masses larger than  $M^*$ , the slope is quickly cutoff by an exponential tail. The overall function is normalized by  $\Phi^*$ , which describes the number density of galaxies at  $M^*$ . For each galaxy sample, we fit a single Schechter function, allowing  $\alpha$ ,  $M^*$ , and  $\Phi^*$  to freely vary, as well as with a fixed  $\alpha = -1.3$ , similar methods adopted by Marchesini et al. (2009); Muzzin et al. (2013); Tomczak et al. (2014). Finally, we show the single Schechter fit derived for the COSMOS2020 field for  $2.5 \leq z \leq 3$  using solely photometry as a comparison with our field sample (Weaver et al. 2023). The fitted values are given in Table 1.

## 5. CONCLUSION AND FUTURE WORK

In this study, we utilized COSMOS2020 photometry, various spectroscopic surveys, and targeted *HST* grism spectroscopy to construct an updated map of the Hyperion proto-supercluster at  $z \sim 2.5$ . By applying the Voronoi Tessellation Monte Carlo (VMC) method to a subsample of this data, we mapped the 3D overdensity distribution of the COSMOS field, identifying the most overdense peaks within Hyperion. We then constructed and compared stellar mass functions (SMFs) of a field galaxy sample to those corresponding to three different density thresholds within Hyperion.

Our findings reveal a consistent trend: decreasing characteristic masses, shallower SMFs, and higher normalizations in the more overdense regions of Hyperion. The increase in normalization is expected, as these regions inherently have a higher galaxy number density. This combination of trends in  $M^*$  and  $\alpha$  leads to a SMF in the most overdense region of Hyperion with a larger fraction of massive galaxies relative to lower-mass ones. This pattern becomes particularly evident after normal-

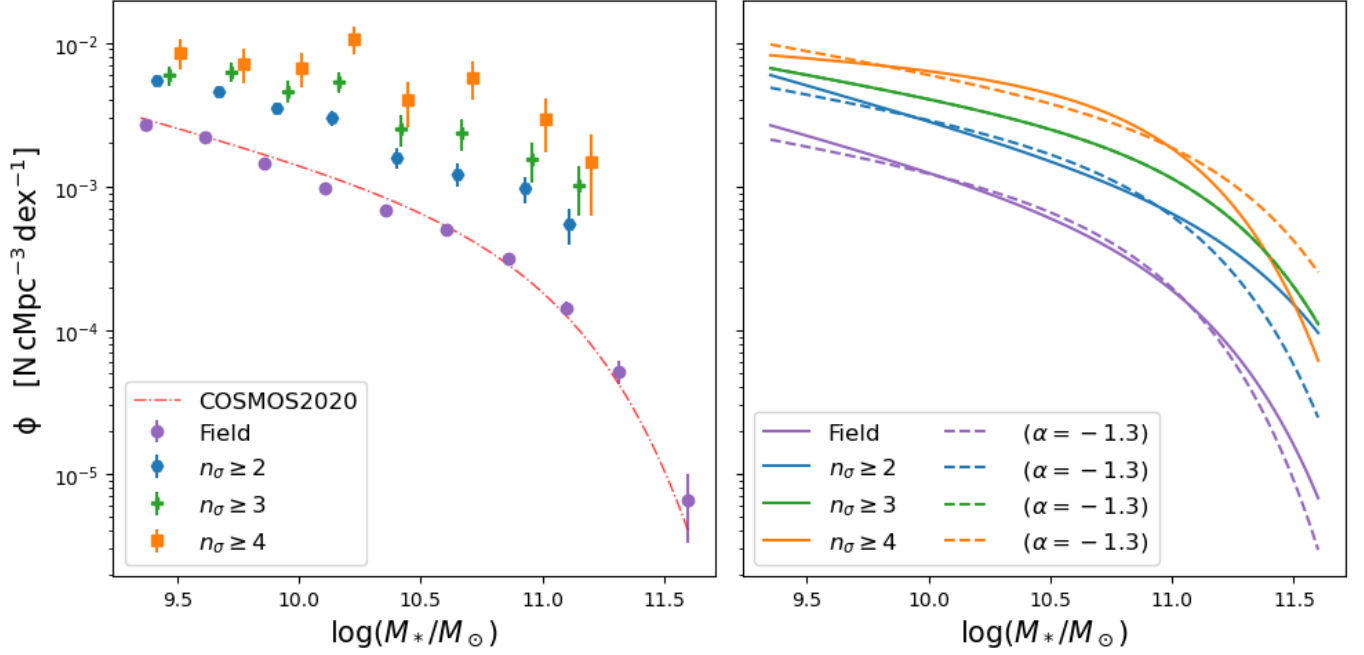


**Figure 9. The Hyperion Stellar Mass Function – Left:** The median SMFs for the 100 MC realizations. We show the SMF for the combined field sample as well as the SMFs of three different overdensity thresholds in Hyperion. **Right:** The single-Schechter function fits. We perform two fits for each SMF, one varying  $\alpha$  and one requiring  $\alpha = -1.3$ .

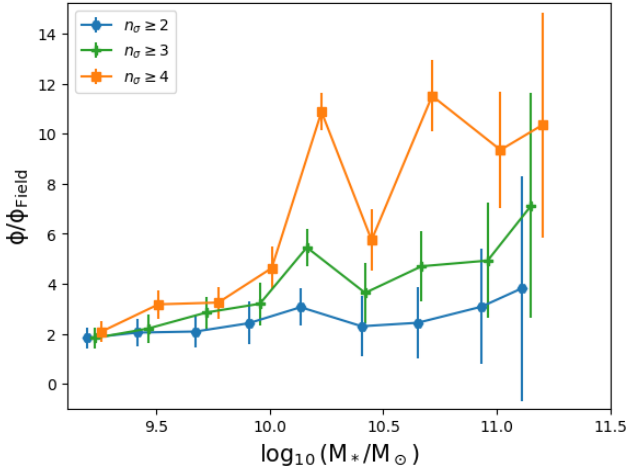


**Figure 10. The Relative Stellar Mass Functions –** We plot the SMFs from Figure 9, but normalized by the Field SMF. There is a clear trend of more enhancement of more massive galaxies in the highest overdensity bins.

izing the SMFs of Hyperion by the field SMF, as shown in Figure 10.

Our observed trend of an increasingly elevated SMF in the overdense regions of Hyperion compared to the field with increasing stellar mass replicates results found in lower redshift ( $z \sim 1$ ) clusters (Tomczak et al. 2017; van der Burg et al. 2018, 2020) as well as higher proto-structures at higher redshifts of  $z \sim 2.5$  (Shimakawa et al. 2018a,b) and  $z \sim 3.3$  (Forrest et al. 2024). Several

physical mechanisms could drive this observed pattern, such as an increased rate of mergers in higher-density regions, leading to the growth of galaxies from lower to higher masses (Tomczak et al. 2017); enhanced star formation rates (SFRs) in more massive galaxies within overdense environments; a greater number of quiescent galaxies (Nantais et al. 2016; van der Burg et al. 2018, 2020); or differences in halo properties between field and Hyperion galaxies (Ahad et al. 2024).

Interestingly, some of these processes are more pronounced in intermediate-density environments rather than in the most extreme overdensities. For instance, Tomczak et al. (2017) demonstrated that galaxy mergers are most efficient in environments where the number density of galaxies is high, but the velocity dispersion remains moderate, facilitating a higher merger rate. In the local universe, the most overdense clusters often exhibit too high a velocity dispersion, limiting merger rates. Instead, mergers are more likely to occur in regions like groups and filaments, which exhibit similar overdensities to the most overdense regions of Hyperion. It is, therefore, plausible that the progenitors of present-day clusters—resembling the most overdense peaks of Hyperion host elevated merger rates, contributing to the excess of massive galaxies observed and potentially driving their eventual quenching.

On the other hand, following the framework of Tomczak et al. (2017), this merger-driven enhancement of

more massive galaxies may result in different shapes for the SMFs of quiescent galaxies in the field and proto-structure environments. While this difference has been observed in some cases (Vulcani et al. 2012; Davidzon et al. 2016; Tomczak et al. 2017), other studies have found little-to-no statistically significant difference between the two quiescent populations (van der Burg et al. 2018, 2020; Edward et al. 2024). Rather, these latter studies argue that the observed difference in the total (i.e., star forming and quiescent combined) SMFs between the field and proto-structure samples is due to an increased fraction of quiescent galaxies in the proto-structure environments. In this scenario, a mass-dependent quenching mechanism which is more efficient at higher stellar masses and in more overdense environments would be needed to explain the similar shapes in the quiescent SMFs between the field and proto-structures. Though the quenching mechanism is still unclear in this scenario, its mass-dependence is a stark difference to what is observed in the local universe (Peng et al. 2010). Finally, it is important to note that these studies define the “field” sample in different ways. Some studies define it as the lowest overdensity regions as we have here (Peng et al. 2010; Tomczak et al. 2017; Forrest

et al. 2024) whereas others have taken it to be an “average” or representative part of the universe at the given epoch (van der Burg et al. 2018, 2020; Edward et al. 2024), which could lead to a biased sample of galaxies which have experienced different levels of environmental effects.

In order to explore this more, the next step will be to compare more of the physical properties of the galaxies in Hyperion with those of the field sample. One example is comparing the SFR of the two samples using the values estimated from our **LePhare** fits or via a UVJ color-color diagram (Williams et al. 2009) to see if there is evidence of a higher quenching fraction in Hyperion. Doing so would also allow us to create and compare SMFs for the quenched galaxies in Hyperion and the field, giving more insight into which of the scenarios described above is observed at  $z \sim 2.5$ . Additionally, we could compare the ages of the two samples using **LePhare**. By examining these and comparing them to similar studies at a wide range of redshifts, we can potentially make a statement about dominant quenching mechanisms in environments like Hyperion based on the timescales over which it happens.

## APPENDIX

### A. FIELD SAMPLES

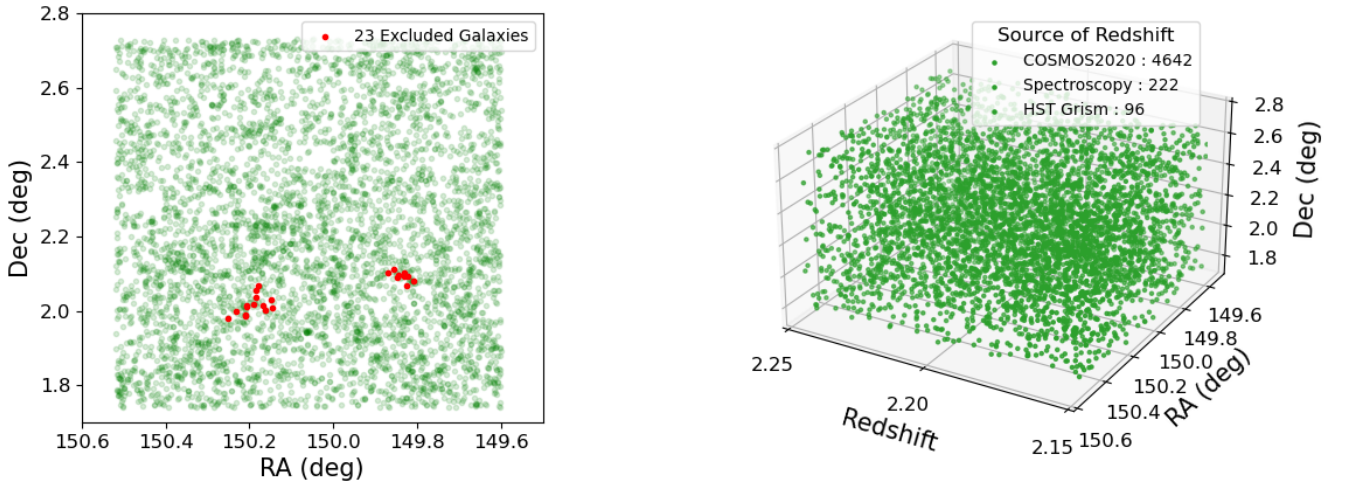


**Figure A1. Lower Redshift Field Sample** – Distribution of the galaxies used to define the lower-redshift ( $2.15 \leq z \leq 2.25$ ) field sample in the sky-projected plane (*left*) and 3D space (*right*). The “excluded galaxies” are galaxies which lay in structures with extremely overdense voxels ( $n_\sigma \geq 4.0$ ) and with total masses  $\log(M/M_\odot) \geq 13.0$ .

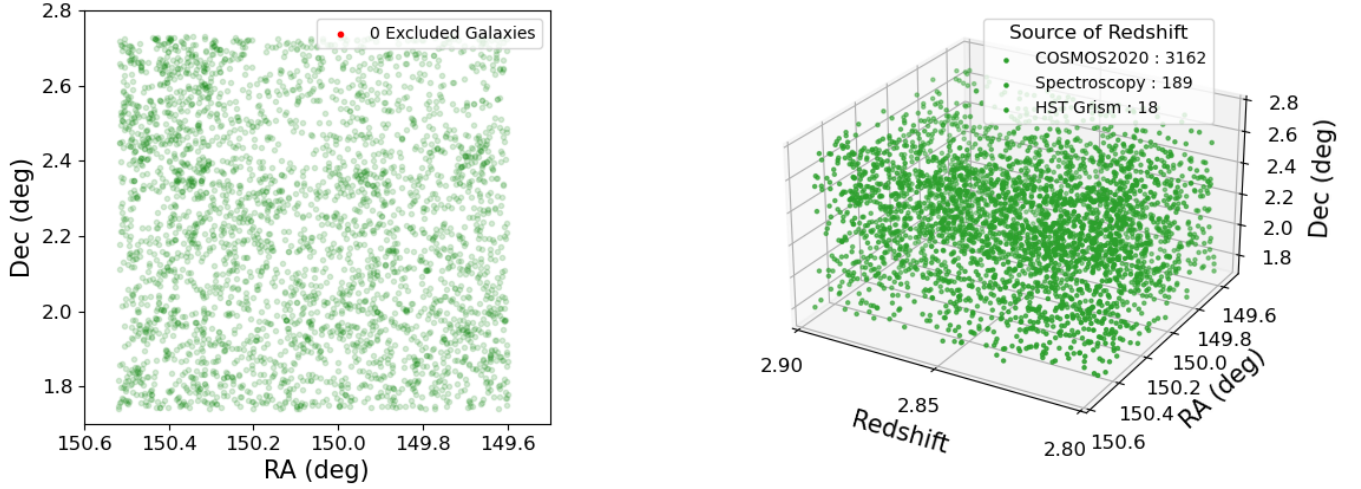


**Figure A2. Higher Redshift Field Sample – Top:** Distribution of the galaxies used to define the higher-redshift ( $2.80 \leq z \leq 2.90$ ) field sample in the sky-projected plane (*left*) and 3D space (*right*). No galaxies are excluded from this sample as there are no extremely overdense structures ( $n_\sigma \geq 4.0$ ) with total masses  $\log(M/M_\odot) \geq 13.0$ .

## B. WHO DID WHAT?

The project idea was conceptualized by RG, BL, and BF. The C3VO spectroscopic data was reduced by BF and the *HST* grism data was reduced by LS and BF. All authors (including DS) with the exception of LL examined the *HST* data by-eye using a GUI developed by LS. The VMC map was produced by BL.

DS created and ran the MC used to better sample the redshift PDFs, refit all of the galaxies in *LePhare* for each iteration, found the overdensity of the galaxy in each realization, and built the SMFs for each realization. DS also wrote the paper under the guidance of the other co-authors.

## REFERENCES

- Abadi, M. G., Moore, B., & Bower, R. G. 1999, MNRAS, 308, 947, doi: [10.1046/j.1365-8711.1999.02715.x](https://doi.org/10.1046/j.1365-8711.1999.02715.x)
- Ahad, S. L., Muzzin, A., Bahé, Y. M., & Hoekstra, H. 2024, MNRAS, 528, 6329, doi: [10.1093/mnras/stae341](https://doi.org/10.1093/mnras/stae341)
- Aihara, H., AlSayyad, Y., Ando, M., et al. 2019, PASJ, 71, 114, doi: [10.1093/pasj/psz103](https://doi.org/10.1093/pasj/psz103)
- Arnouts, S., Cristiani, S., Moscardini, L., et al. 1999, MNRAS, 310, 540, doi: [10.1046/j.1365-8711.1999.02978.x](https://doi.org/10.1046/j.1365-8711.1999.02978.x)
- Arnouts, S., Le Floc’h, E., Chevallard, J., et al. 2013, A&A, 558, A67, doi: [10.1051/0004-6361/201321768](https://doi.org/10.1051/0004-6361/201321768)
- Ashby, M. L. N., Willner, S. P., Fazio, G. G., et al. 2013, ApJ, 769, 80, doi: [10.1088/0004-637X/769/1/80](https://doi.org/10.1088/0004-637X/769/1/80)
- . 2015, ApJS, 218, 33, doi: [10.1088/0067-0049/218/2/33](https://doi.org/10.1088/0067-0049/218/2/33)
- Ashby, M. L. N., Caputi, K. I., Cowley, W., et al. 2018, ApJS, 237, 39, doi: [10.3847/1538-4365/aad4fb](https://doi.org/10.3847/1538-4365/aad4fb)
- Ata, M., Lee, K.-G., Vecchia, C. D., et al. 2022, Nature Astronomy, 6, 857, doi: [10.1038/s41550-022-01693-0](https://doi.org/10.1038/s41550-022-01693-0)
- Azzalini, A. 1985, Scandinavian Journal of Statistics, 12, 171. <http://www.jstor.org/stable/4615982>
- Azzalini, A., & Capitanio, A. 2009, arXiv e-prints, arXiv:0911.2093, doi: [10.48550/arXiv.0911.2093](https://doi.org/10.48550/arXiv.0911.2093)
- Béthermin, M., Daddi, E., Magdis, G., et al. 2012, ApJL, 757, L23, doi: [10.1088/2041-8205/757/2/L23](https://doi.org/10.1088/2041-8205/757/2/L23)
- Bruzual, G., & Charlot, S. 2003, MNRAS, 344, 1000, doi: [10.1046/j.1365-8711.2003.06897.x](https://doi.org/10.1046/j.1365-8711.2003.06897.x)
- Calzetti, D., Armus, L., Bohlin, R. C., et al. 2000, ApJ, 533, 682, doi: [10.1086/308692](https://doi.org/10.1086/308692)
- Casey, C. M., Cooray, A., Capak, P., et al. 2015, ApJL, 808, L33, doi: [10.1088/2041-8205/808/2/L33](https://doi.org/10.1088/2041-8205/808/2/L33)
- Chabrier, G. 2003, PASP, 115, 763, doi: [10.1086/376392](https://doi.org/10.1086/376392)
- Chiang, Y.-K., Overzier, R. A., Gebhardt, K., et al. 2015, ApJ, 808, 37, doi: [10.1088/0004-637X/808/1/37](https://doi.org/10.1088/0004-637X/808/1/37)
- Cucciati, O., Zamorani, G., Lemaux, B. C., et al. 2014, A&A, 570, A16, doi: [10.1051/0004-6361/201423811](https://doi.org/10.1051/0004-6361/201423811)
- Cucciati, O., Lemaux, B. C., Zamorani, G., et al. 2018, A&A, 619, A49, doi: [10.1051/0004-6361/201833655](https://doi.org/10.1051/0004-6361/201833655)
- Davidzon, I., Cucciati, O., Bolzonella, M., et al. 2016, A&A, 586, A23, doi: [10.1051/0004-6361/201527129](https://doi.org/10.1051/0004-6361/201527129)



- Dekel, A., & Birnboim, Y. 2006, *MNRAS*, 368, 2, doi: [10.1111/j.1365-2966.2006.10145.x](https://doi.org/10.1111/j.1365-2966.2006.10145.x)
- Dekel, A., & Silk, J. 1986, *ApJ*, 303, 39, doi: [10.1086/164050](https://doi.org/10.1086/164050)
- Diener, C., Lilly, S. J., Ledoux, C., et al. 2015, *ApJ*, 802, 31, doi: [10.1088/0004-637X/802/1/31](https://doi.org/10.1088/0004-637X/802/1/31)
- Durkalec, A., Le Fèvre, O., Pollo, A., et al. 2015, *A&A*, 583, A128, doi: [10.1051/0004-6361/201425343](https://doi.org/10.1051/0004-6361/201425343)
- Edward, A. H., Balogh, M. L., Bahé, Y. M., et al. 2024, *MNRAS*, 527, 8598, doi: [10.1093/mnras/stad3751](https://doi.org/10.1093/mnras/stad3751)
- Faber, S. M., Phillips, A. C., Kibrick, R. I., et al. 2003, in *Society of Photo-Optical Instrumentation Engineers (SPIE) Conference Series*, Vol. 4841, *Instrument Design and Performance for Optical/Infrared Ground-based Telescopes*, ed. M. Iye & A. F. M. Moorwood, 1657–1669, doi: [10.1117/12.460346](https://doi.org/10.1117/12.460346)
- Forrest, B., Tran, K.-V. H., Broussard, A., et al. 2017, *ApJL*, 838, L12, doi: [10.3847/2041-8213/aa653b](https://doi.org/10.3847/2041-8213/aa653b)
- Forrest, B., Lemaux, B. C., Shah, E., et al. 2023, *MNRAS*, 526, L56, doi: [10.1093/mnras/slad114](https://doi.org/10.1093/mnras/slad114)
- Forrest, B., Lemaux, B. C., Shah, E. A., et al. 2024, *arXiv e-prints*, arXiv:2405.18491, doi: [10.48550/arXiv.2405.18491](https://doi.org/10.48550/arXiv.2405.18491)
- Fukugita, M., Ichikawa, T., Gunn, J. E., et al. 1996, *AJ*, 111, 1748, doi: [10.1086/117915](https://doi.org/10.1086/117915)
- Gaia Collaboration, Brown, A. G. A., Vallenari, A., et al. 2016, *A&A*, 595, A2, doi: [10.1051/0004-6361/201629512](https://doi.org/10.1051/0004-6361/201629512)
- . 2018, *A&A*, 616, A1, doi: [10.1051/0004-6361/201833051](https://doi.org/10.1051/0004-6361/201833051)
- Hasinger, G., Capak, P., Salvato, M., et al. 2018, *ApJ*, 858, 77, doi: [10.3847/1538-4357/aabacf](https://doi.org/10.3847/1538-4357/aabacf)
- Hoaglin, D. C., Mosteller, F., & Tukey, J. W. 1983, *Understanding robust and exploratory data analysis*
- Hung, D., Lemaux, B. C., Gal, R. R., et al. 2020, *MNRAS*, 491, 5524, doi: [10.1093/mnras/stz3164](https://doi.org/10.1093/mnras/stz3164)
- Ilbert, O., Arnouts, S., McCracken, H. J., et al. 2006, *A&A*, 457, 841, doi: [10.1051/0004-6361:20065138](https://doi.org/10.1051/0004-6361:20065138)
- Ilbert, O., Capak, P., Salvato, M., et al. 2009, *ApJ*, 690, 1236, doi: [10.1088/0004-637X/690/2/1236](https://doi.org/10.1088/0004-637X/690/2/1236)
- Ilbert, O., Arnouts, S., Le Floc’h, E., et al. 2015, *A&A*, 579, A2, doi: [10.1051/0004-6361/201425176](https://doi.org/10.1051/0004-6361/201425176)
- Kawinwanichakij, L., Papovich, C., Quadri, R. F., et al. 2017, *ApJ*, 847, 134, doi: [10.3847/1538-4357/aa8b75](https://doi.org/10.3847/1538-4357/aa8b75)
- Kennicutt, Robert C., J. 1998, *ARA&A*, 36, 189, doi: [10.1146/annurev.astro.36.1.189](https://doi.org/10.1146/annurev.astro.36.1.189)
- Laigle, C., McCracken, H. J., Ilbert, O., et al. 2016, *ApJS*, 224, 24, doi: [10.3847/0067-0049/224/2/24](https://doi.org/10.3847/0067-0049/224/2/24)
- Le Fèvre, O., Vettolani, G., Garilli, B., et al. 2005, *A&A*, 439, 845, doi: [10.1051/0004-6361:20041960](https://doi.org/10.1051/0004-6361:20041960)
- Le Fèvre, O., Tasca, L. A. M., Cassata, P., et al. 2015, *A&A*, 576, A79, doi: [10.1051/0004-6361/201423829](https://doi.org/10.1051/0004-6361/201423829)
- Leauthaud, A., Massey, R., Kneib, J.-P., et al. 2007, *ApJS*, 172, 219, doi: [10.1086/516598](https://doi.org/10.1086/516598)
- Lee, K.-G., Hennawi, J. F., White, M., et al. 2016, *ApJ*, 817, 160, doi: [10.3847/0004-637X/817/2/160](https://doi.org/10.3847/0004-637X/817/2/160)
- Lemaux, B. C., Cucciati, O., Tasca, L. A. M., et al. 2014, *A&A*, 572, A41, doi: [10.1051/0004-6361/201423828](https://doi.org/10.1051/0004-6361/201423828)
- Lemaux, B. C., Le Fèvre, O., Cucciati, O., et al. 2018, *A&A*, 615, A77, doi: [10.1051/0004-6361/201730870](https://doi.org/10.1051/0004-6361/201730870)
- Lemaux, B. C., Cucciati, O., Le Fèvre, O., et al. 2022, *A&A*, 662, A33, doi: [10.1051/0004-6361/202039346](https://doi.org/10.1051/0004-6361/202039346)
- Lilly, S. J., Le Fèvre, O., Renzini, A., et al. 2007, *ApJS*, 172, 70, doi: [10.1086/516589](https://doi.org/10.1086/516589)
- Lin, L., Cooper, M. C., Jian, H.-Y., et al. 2010, *ApJ*, 718, 1158, doi: [10.1088/0004-637X/718/2/1158](https://doi.org/10.1088/0004-637X/718/2/1158)
- Lubin, L. M., Gal, R. R., Lemaux, B. C., Kocevski, D. D., & Squires, G. K. 2009, *AJ*, 137, 4867, doi: [10.1088/0004-6256/137/6/4867](https://doi.org/10.1088/0004-6256/137/6/4867)
- Marchesini, D., van Dokkum, P. G., Förster Schreiber, N. M., et al. 2009, *ApJ*, 701, 1765, doi: [10.1088/0004-637X/701/2/1765](https://doi.org/10.1088/0004-637X/701/2/1765)
- McConachie, I., Wilson, G., Forrest, B., et al. 2022, *ApJ*, 926, 37, doi: [10.3847/1538-4357/ac2b9f](https://doi.org/10.3847/1538-4357/ac2b9f)
- McCracken, H. J., Milvang-Jensen, B., Dunlop, J., et al. 2012, *A&A*, 544, A156, doi: [10.1051/0004-6361/201219507](https://doi.org/10.1051/0004-6361/201219507)
- McLean, I. S., Steidel, C. C., Epps, H. W., et al. 2012, in *Society of Photo-Optical Instrumentation Engineers (SPIE) Conference Series*, Vol. 8446, *Ground-based and Airborne Instrumentation for Astronomy IV*, ed. I. S. McLean, S. K. Ramsay, & H. Takami, 84460J, doi: [10.1117/12.924794](https://doi.org/10.1117/12.924794)
- Moneti, A., McCracken, H. J., Hudelot, W., et al. 2023, *VizieR Online Data Catalog: The fourth UltraVISTA data release (DR4) (Moneti+, 2019), VizieR On-line Data Catalog: II/373. Originally published in: 2012A&A...544A.156M*
- Muzzin, A., Marchesini, D., Stefanon, M., et al. 2013, *ApJ*, 777, 18, doi: [10.1088/0004-637X/777/1/18](https://doi.org/10.1088/0004-637X/777/1/18)
- Nantais, J. B., van der Burg, R. F. J., Lidman, C., et al. 2016, *A&A*, 592, A161, doi: [10.1051/0004-6361/201628663](https://doi.org/10.1051/0004-6361/201628663)
- Oke, J. B., & Gunn, J. E. 1983, *ApJ*, 266, 713, doi: [10.1086/160817](https://doi.org/10.1086/160817)
- Papovich, C., Kawinwanichakij, L., Quadri, R. F., et al. 2018, *ApJ*, 854, 30, doi: [10.3847/1538-4357/aaa766](https://doi.org/10.3847/1538-4357/aaa766)
- Peng, Y.-j., Lilly, S. J., Kovač, K., et al. 2010, *ApJ*, 721, 193, doi: [10.1088/0004-637X/721/1/193](https://doi.org/10.1088/0004-637X/721/1/193)
- Sawicki, M., Arnouts, S., Huang, J., et al. 2019, *MNRAS*, 489, 5202, doi: [10.1093/mnras/stz2522](https://doi.org/10.1093/mnras/stz2522)
- Schechter, P. 1976, *ApJ*, 203, 297, doi: [10.1086/154079](https://doi.org/10.1086/154079)

- Scoville, N., Aussel, H., Brusa, M., et al. 2007, *ApJS*, 172, 1, doi: [10.1086/516585](https://doi.org/10.1086/516585)
- Shah, E. A., Lemaux, B., Forrest, B., et al. 2024, *MNRAS*, 529, 873, doi: [10.1093/mnras/stae519](https://doi.org/10.1093/mnras/stae519)
- Shen, L., Lemaux, B. C., Lubin, L. M., et al. 2021, *ApJ*, 912, 60, doi: [10.3847/1538-4357/abee75](https://doi.org/10.3847/1538-4357/abee75)
- Shimakawa, R., Kodama, T., Hayashi, M., et al. 2018a, *MNRAS*, 473, 1977, doi: [10.1093/mnras/stx2494](https://doi.org/10.1093/mnras/stx2494)
- Shimakawa, R., Koyama, Y., Röttgering, H. J. A., et al. 2018b, *MNRAS*, 481, 5630, doi: [10.1093/mnras/sty2618](https://doi.org/10.1093/mnras/sty2618)
- Somerville, R. S., Hopkins, P. F., Cox, T. J., Robertson, B. E., & Hernquist, L. 2008, *MNRAS*, 391, 481, doi: [10.1111/j.1365-2966.2008.13805.x](https://doi.org/10.1111/j.1365-2966.2008.13805.x)
- Staab, P., Lemaux, B. C., Forrest, B., et al. 2024, *MNRAS*, 528, 6934, doi: [10.1093/mnras/stae301](https://doi.org/10.1093/mnras/stae301)
- Steidel, C. C., Adelberger, K. L., Dickinson, M., et al. 1998, *ApJ*, 492, 428, doi: [10.1086/305073](https://doi.org/10.1086/305073)
- Steinhardt, C. L., Speagle, J. S., Capak, P., et al. 2014, *ApJL*, 791, L25, doi: [10.1088/2041-8205/791/2/L25](https://doi.org/10.1088/2041-8205/791/2/L25)
- Taniguchi, Y., Scoville, N., Murayama, T., et al. 2007, *ApJS*, 172, 9, doi: [10.1086/516596](https://doi.org/10.1086/516596)
- Taniguchi, Y., Kajisawa, M., Kobayashi, M. A. R., et al. 2015, *PASJ*, 67, 104, doi: [10.1093/pasj/psv106](https://doi.org/10.1093/pasj/psv106)
- Tomczak, A. R., Quadri, R. F., Tran, K.-V. H., et al. 2014, *ApJ*, 783, 85, doi: [10.1088/0004-637X/783/2/85](https://doi.org/10.1088/0004-637X/783/2/85)
- Tomczak, A. R., Lemaux, B. C., Lubin, L. M., et al. 2017, *MNRAS*, 472, 3512, doi: [10.1093/mnras/stx2245](https://doi.org/10.1093/mnras/stx2245)
- van der Burg, R. F. J., McGee, S., Aussel, H., et al. 2018, *A&A*, 618, A140, doi: [10.1051/0004-6361/201833572](https://doi.org/10.1051/0004-6361/201833572)
- van der Burg, R. F. J., Rudnick, G., Balogh, M. L., et al. 2020, *A&A*, 638, A112, doi: [10.1051/0004-6361/202037754](https://doi.org/10.1051/0004-6361/202037754)
- Virtanen, P., Gommers, R., Oliphant, T. E., et al. 2020, *Nature Methods*, 17, 261, doi: [10.1038/s41592-019-0686-2](https://doi.org/10.1038/s41592-019-0686-2)
- Vulcani, B., Poggianti, B. M., Fasano, G., et al. 2012, *MNRAS*, 420, 1481, doi: [10.1111/j.1365-2966.2011.20135.x](https://doi.org/10.1111/j.1365-2966.2011.20135.x)
- Wang, T., Elbaz, D., Daddi, E., et al. 2016, *ApJ*, 828, 56, doi: [10.3847/0004-637X/828/1/56](https://doi.org/10.3847/0004-637X/828/1/56)
- Weaver, J. R., Kauffmann, O. B., Ilbert, O., et al. 2022, *ApJS*, 258, 11, doi: [10.3847/1538-4365/ac3078](https://doi.org/10.3847/1538-4365/ac3078)
- Weaver, J. R., Davidzon, I., Toft, S., et al. 2023, *A&A*, 677, A184, doi: [10.1051/0004-6361/202245581](https://doi.org/10.1051/0004-6361/202245581)
- Webb, K., Balogh, M. L., Leja, J., et al. 2020, *MNRAS*, 498, 5317, doi: [10.1093/mnras/staa2752](https://doi.org/10.1093/mnras/staa2752)
- Williams, R. J., Quadri, R. F., Franx, M., van Dokkum, P., & Labbé, I. 2009, *ApJ*, 691, 1879, doi: [10.1088/0004-637X/691/2/1879](https://doi.org/10.1088/0004-637X/691/2/1879)
- Zamojski, M. A., Schiminovich, D., Rich, R. M., et al. 2007, *ApJS*, 172, 468, doi: [10.1086/516593](https://doi.org/10.1086/516593)